Numerical Simulation of Magnetic Nano Drug Targeting in a Patient-Specific Coeliac Trunk. ☆

Andrea Boghi[a,*], Flavia Russo[b], Fabio Gori[b]

[a]*School of Energy, Environment and Agrifood, Cranfield University, Cranfield, Bedfordshire MK43 0AL, United Kingdom*
[b]*Department of Mechanical Engineering, University of Rome Tor Vergata, Via del Politecnico 1, 00133 Rome, Italy*

Abstract

Magnetic nano drug targeting, through the use of an external magnetic field, is a new technique for the treatment of several diseases, which can potentially avoid the dispersion of drugs in undesired locations of the body. Nevertheless, due to the limitations on the intensity of the magnetic field applied, the hydrodynamic forces can reduce the effectiveness of the procedure. This technique is studied in this paper with the Computational Fluid Dynamics (CFD), focusing on the influence of the magnetic probe position, and the direction of the circulating electric current. A single rectangular coil is used to generate the external magnetic field. A patient-specific geometry of the coeliac trunk is reconstructed from DICOM images, with the use of VMTK. A new solver, coupling the Lagrangian dynamics of the nanoparticles with the Eulerian dynamics of the blood, is implemented in OpenFOAM to perform the simulations. The resistive pressure, the Womersley's profile for the inlet velocity and the magnetic field of a rectangular coil are implemented in the software as boundary conditions. The results show the influence of the position of the probe, as well as the limitations associated with the rectangular coil configuration.

Keywords: Magnetic Hydro Dynamics, Patient-Specific, Nanoparticles, Lagrangian model, Eulerian model, Coeliac Trunk.

1. Introduction

The liver tumor results from a quick proliferation of the cells. The primary hepatic tumors, called hepatocellular tumors, are born inside the hepatic cells and spread towards bones and lungs. It is a rare condition but its mortality is quite high, as the World Health Organization has reported a number of death

---

☆Nano Drug Targeting in Coeliac Trunk

*A. Boghi
  Email address: a.boghi@cranfield.ac.uk (Andrea Boghi)

equals to 745.000 during 2012, which is the second cause of death among common cancers. Moreover, it is mostly widespread in Asia, accounting for 782.000 new cancer cases only in 2012. A smaller number of cases per year is reported in USA and Europe, e.g. in Southern Europe the incidence is 9.5% and in Northern Europe only 4.6%, which can be compared to 2% of overall tumors [1]. Nowadays, it is impossible to prevent this disease except avoiding the main risk factors, such as alcohol excess and hepatitis viruses. Chemotherapy can ensure a good quality of life, avoiding the spread of the metastasis. However, these drug treatments can have numerous hazardous side effects.

In the last few years, new technologies have been developed in order to decrease these undesired side effects. In the magnetic drug delivery the drugs are guided directly to the interested regions of the body and the absorption in other organs, or systems, not interested by the tumor, decreases, which results in a higher quality of life of the patient.

The study of Magneto Hydro Dynamics (MHD) started in the late 30s by Hartmann and Lazarus [2], who investigated the flow of an incompressible Newtonian fluid inside a duct, under the influence of an external magnetic field. The first analytical characterization of the problem has been done by Shercliff at the end of the 50s [3], who, later on, investigated the flow at high Hartmann numbers [4]. At the beginning of the 60s, Gold [5] obtained the solution for the steady one-dimensional flow of an incompressible, viscous, electrically conducting fluid, through a circular pipe, in presence of an applied uniform magnetic field. The early studies were performed for liquid metals, and only in the 90s the research was extended to biological fluids [6, 7]. Several applications in bioengineering and medicine have been developed since then. Among them, the targeted transport of drugs by external magnetic fields and magnetic tracers are of particular interest [3, 8].

The blood is the most important biological fluid, composed by plasma and erythrocytes, which contain hemoglobin, whose main molecule is iron. The presence of this element allows the blood to be magnetized in presence of an electromagnetic field. In the deoxygenated state, the blood behaves as a paramagnetic material with a magnetic susceptibility of $\chi = 3.5 \cdot 10^{-6}$, while, in the oxygenated state, the blood is diamagnetic and its susceptibility is $\chi = -6.6 \cdot 10^{-7}$ [9].

Several studies have been conducted to investigate the blood velocity profile inside the human circulatory system, both for healthy and non-healthy patients. In the last decades, some experimental data have been compared with numerical results, obtained with the Computational Fluid Dynamics (CFD), a technique well established in biomedical applications [10–16]. The influence of geometrical factors on pathological conditions has been investigated, suggesting that the most important factor to be taken into account is the velocity field, whose measurements can be provided by Doppler Ultra Sound and MRI [17, 18]. Long et al. [19] reconstructed the blood flow in the carotid bifurcation from MRI images. Moreover, Moulinier et al. [18] used the Doppler echocardiography to get information on the blood flow in the aortic arch.

Some studies investigated the effect of the magnetic field on metal nanopar-

2

ticles embedded in the blood flow, and their use as drug carriers [20–22]. Other investigations on drug delivery have been performed on non-biological fluid [17] and on clinical trials of cancer patients [23, 24]. A few CFD studies have been conducted to simulate the magnetic drug targeting. In [25], the behavior of magnetic particles in blood vessels and surrounding tissue has been analyzed in a cylindrical geometry by solving the particle concentration and including a "magnetic drift" term. In [26], a numerical simulations of blood flow and magnetic drug carrier distributions in a patient-specific brain vascular system has been reported. The blood was represented as a non-Newtonian power-law fluid, neglecting the influence of the Lorentz force. A Lagrangian approach was used to simulate the particle tracking, neglecting the buoyancy and the carrier phase inertia. The Lorentz force has been introduced in [27], with a Lagrangian particle tracking algorithm to simulate magnetic drug delivery in a two-dimensional bifurcation. In [28], the nanoparticle sticking-steering relationship has been investigated using Lagrangian particle tracking. In [29, 30], magnetic drug delivery has been studied in a three-dimensional bifurcation using Lagrangian particle tracking.

The present study investigates the fluid dynamics of blood in the coeliac trunk, where nanoparticles, used for drug targeting, are dragged into the liver by an external magnetic field. A patient-specific geometry is reconstructed from a data set of CT scan images of a middle-aged healthy man. The blood is treated as a continuum medium and therefore an Eulerian formulation is employed to describe it, while the nanoparticles are treated with a Lagrangian approach. A rectangular coil is employed as source of the external magnetic field. The influence of the probe position and the current intensity are investigated.

2. Materials and Methods

2.1. Domain reconstruction

The geometrical model is made with the open-source software VMTK (The Vascular Modelling Toolkit) [31], which reconstructs a real artery from a DICOM series of images. Since the procedure is operator-dependent, the non-interesting structures and artefacts are removed manually. The Level Set Segmentation algorithm is applied to reconstruct the surface of the artery [6], which is refined with the parametric deformable models, initialized with the Colliding Front methodology. The output of the Level Set Segmentation algorithm is an image, and the Marching Cubes algorithm is used to reconstruct the surface, due to the depth of the interested vessel.

Flow extensions of cylindrical shapes are added at the inlets and outlets of the domain, to ensure that the flow, entering and leaving the computational domain, is fully developed. In this work, the length of each flow extension has been set equal to 3 times its diameter. This approach allows using standard boundary conditions (BC) to solve the partial differential equations (PDE) governing the phenomenon. Once the flow extensions are added, the computational grid, which solves the discretized equations, is generated [6].
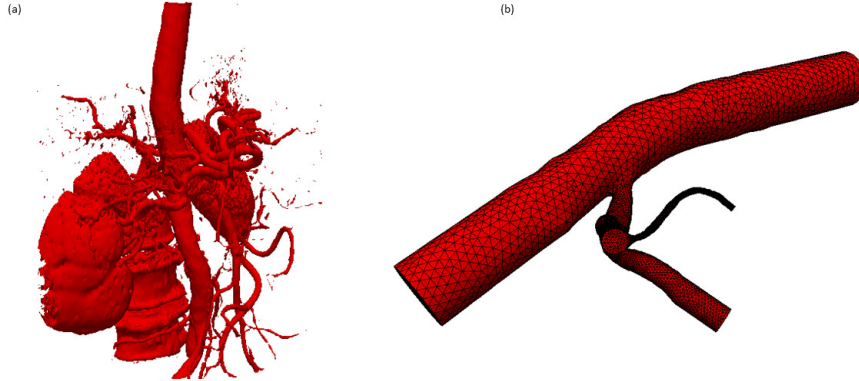
3

Figure 1: (a) Application of the Marching Cubes algorithm to obtain a reconstruction of the Abdominal Aorta with its collateral structures; (b) Detail of the geometry used in this study.

An adaptive mesh is generated in order to have a more refined grid close to the wall. Refinement is requested for the coeliac trunk, since the dimensions of its branches are smaller than the Thoracic Aorta (TA). Tetrahedral elements are used for the computational grid. The minimum and maximum dihedral angles are set up in order to reduce the skew angle and the number of non-orthogonal cells. Three grids are created with different number of elements, respectively $183, 498$ (grid1), $324, 577$ (grid2) and $626, 875$ (grid3), to verify that the numerical solutions are grid-independent.

The domain is shown in Fig.(1), where Fig.(1,a) presents the reconstruction obtained with the application of the Marching Cubes algorithm, while Fig.(1,b) shows the segments used for the numerical simulations. The three main branches of the coeliac trunk, i.e. Left Gastric Artery (LGA), Common Hepatic Artery (CHA), and Splenic Artery (SA) are represented.

2.2. Eulerian Model

The MHD mathematical model is based on the coupling between the Navier-Stokes equations and the Maxwell ones. It is known that an external magnetic field can change the direction of a moving charged particle, and the force responsible for it is known as the Lorentz force [32]. The MHD equations can be written for incompressible flow of a viscous, conducting liquid

$$\text{div} \left(\vec{v}_b \right) = 0 \tag{1}$$

$$\frac{\partial \vec{v}_b}{\partial t} + (\vec{v}_b \cdot \nabla)\,\vec{v}_b = -\frac{1}{\rho_b}\nabla p + \nu_b \nabla^2 \vec{v}_b + \vec{g} + \frac{1}{\rho_b \mu_0}\mathrm{curl}\left(\vec{B}\right) \times \vec{B} \qquad (2)$$

$$\frac{\partial \vec{B}}{\partial t} + (\vec{v}_b \cdot \nabla)\,\vec{B} = \left(\vec{B} \cdot \nabla\right)\vec{v}_b + \frac{1}{\sigma_b \mu_0}\nabla^2 \vec{B} \qquad (3)$$

where the subscript b denotes blood, ν_b is the kinematic viscosity, ρ_b the density, μ_0 the magnetic permeability in the vacuum, which is approximately the same of the blood, σ_b the electric conductivity, $\vec{g}$ the gravity acceleration, p the static pressure, $\vec{v}_b$ the velocity field, and $\vec{B}$ the magnetic induction field.

The momentum conservation equation, Eq.(2), does not take into account the momentum which the particles transfer to the blood and the last term represents the Lorentz force in the context of continuum mechanics. According to [33, 34] for particle volume fractions less than 10^{-6}, particle motion is influenced by continuous phase properties while practically there is no feedback from the dispersed phase.

The particle diameter used in this work is 5nm, which is typical of gold/iron-oxide nanoparticles [35, 36]. Therefore, we assumed that the inertia of the magnetic particles is much smaller than the blood, which is justified by their small volume of the order of 65nm^3.

2.3. Lagrangian Model

A particle of diameter d_p, velocity $\vec{v}_p$, and density ρ_p, is defined by the position of its center, $\vec{x}_p$. In a Lagrangian frame of reference, the position of each particle is obtained by the integration of its velocity,

$$\frac{d\vec{x}_p}{dt} = \vec{v}_p \qquad (4)$$

which is evaluated from the momentum conservation equation, written as follows

$$\frac{d\vec{v}_p}{dt} = -\underbrace{\frac{1}{\tau_p}\left(\vec{v}_p - \vec{v}_b + \frac{d_p^2}{12}\nabla^2 \vec{v}_b\right)}_{(I)} + \underbrace{\left(1 - \frac{\rho_b}{\rho_p}\right)\vec{g}}_{(II)} + \underbrace{\frac{\rho_b}{\rho_p}\left(\frac{\partial \vec{v}_b}{\partial t} + (\vec{v}_b \cdot \nabla)\,\vec{v}_b\right)}_{(III)} +$$

$$\underbrace{\frac{1}{2}\frac{\rho_b}{\rho_p}\left(\frac{\partial \vec{v}_b}{\partial t} + (\vec{v}_b \cdot \nabla)\,\vec{v}_b - \frac{d\vec{v}_p}{dt}\right)}_{(IV)} + \underbrace{\left(\frac{q_p}{m_p}\vec{v}_p - \frac{1}{\rho_p \mu_0}\mathrm{curl}\left(\vec{B}\right)\right) \times \vec{B}}_{(V)} \qquad (5)$$

Where (I) is the drag term, (II) is the buoyancy, (III) is the carrier phase inertia, (IV) is the added mass and (V) is the Lorentz force. It must be noted that in Eq.(5) we have neglected the particle-particle interactions. This assumption has been made because of the small volume of the particles, which reduces the probability of collision. Moreover, the intra-particle interactions are computationally demanding, and dont seem to be important in this study.

Furthermore, q_p is the electric charge of the particle, m_p its mass and τ_p the relaxation time of the particle, defined as

$$\tau_p = \frac{4}{3} \frac{\rho_p d_p}{\rho_b C_d \left| \vec{v}_b - \vec{v}_p \right|} \tag{6}$$

The standard definition of the drag coefficient, according to the derivation from Schiller and Neumann [37], is the following

$$C_d = \begin{cases} \frac{24}{\mathrm{Re_p}} & \mathrm{Re_p} < 0.1 \\ \frac{24}{\mathrm{Re_p}} \left(1 + \frac{1}{6} \mathrm{Re_p^{2/3}} \right) & 0.1 < \mathrm{Re_p} < 1000 \\ 0.44 & \mathrm{Re_p} > 1000 \end{cases} \tag{7}$$

The particle Reynolds number is

$$\mathrm{Re}_p = \frac{d_p \left| \vec{v}_b - \vec{v}_p \right|}{\nu_b} \tag{8}$$

2.4. Boundary Conditions (BC)

The solution of the Eulerian system requires appropriate boundary conditions (BC) for each field. A non-slip BC has been imposed for the velocity at the wall. As far as the outlets are concerned, a mixed BC has been used. If the blood leaves the domain, the velocity normal derivative is set to zero, whereas if blood enters through the boundary, the tangential velocity is set to zero. The velocity profile is imposed on the inlet. In the steady state a parabolic profile is used, whereas in unsteady state a Womersley-Evans profile is employed, in analogy with [14].

$$v_b \left(t, \xi \right) = 8 \frac{Q}{\pi D^2} \left(1 - \xi^2 \right) + 2 \Re \left(\sum_{n=1}^{N} V_n \Phi \left(\tau_n, \xi \right) e^{j \omega_n t} \right) \tag{9}$$

where

$$\Phi \left(\tau_n, \xi \right) = \frac{J_0 \left(\tau_n \right) - J_0 \left(\tau_n \xi \right)}{J_0 \left(\tau_n \right) - 2 J_1 \left(\tau_n \right) / \tau_n} \tag{10}$$

and

$$\tau_n = j^{\frac{3}{2}} \frac{D}{2} \sqrt{\frac{\rho}{\mu_\infty} \omega_n} = j^{\frac{3}{2}} \alpha_n \tag{11}$$

Being r the radial coordinate, D the diameter of the ascending Aorta, Q the volumetric flow rate, $\xi = 2r/D$, J_0 and J_1 the zeroth and first-order Bessel functions of the first kind, α_n the Womersley numbers of order n, $\Re \left(\right)$ the real part of a complex number, $j = \sqrt{-1}$, V_n the Fourier coefficients of the pulsatile mean velocity profile and the number of harmonics used to reproduce the flow rate. The first ten Fourier coefficients of the flow rate in the ascending aorta are used to reconstruct the velocity profile, according to the experiments [38]. The reconstructed flow rate is shown in Fig.(2)
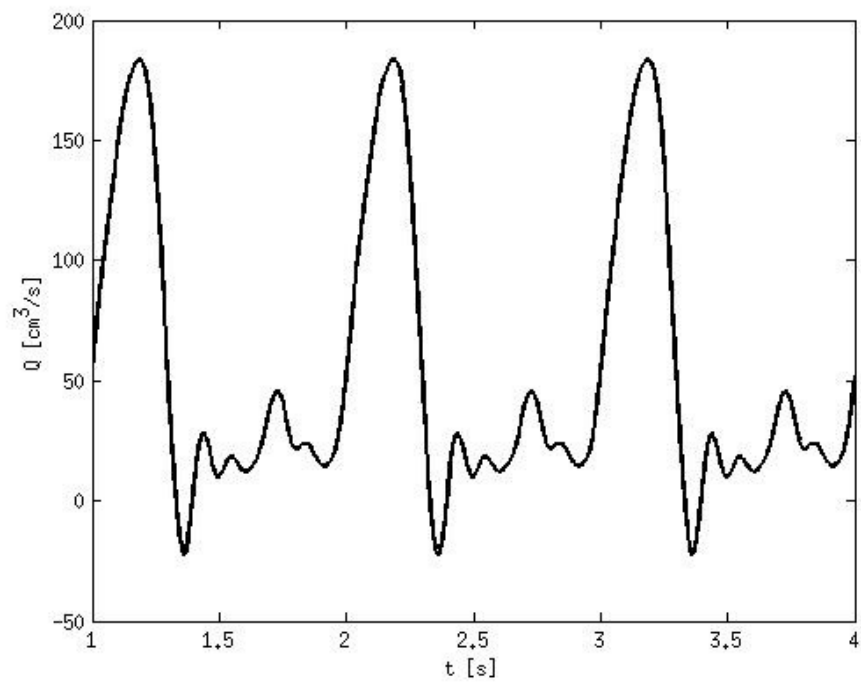
Figure 2: Aorta's Volumetric Flow Rate vs time.

As far as the pressure is concerned, a constant total value, equal to the sum of the static and dynamic ones, is imposed on the outlet of the Abdominal Aorta (AA). On the other outlets the resistive BC, derived in [39], is used

$$p = p_b + RQ \tag{12}$$

being p_b the reference pressure at the right atrium and R the hydraulic resistance. The value of the resistance and the reference pressure are extrapolated from the steady state simulations by imposing the volumetric flow rates and a zero normal derivative for the pressure. The values of the flow rates, in steady state, for the different outlets are derived from the literature [40–42].

2.5. Magnetic Induction BC

As far as the magnetic induction field is concerned, the normal derivative are set to zero everywhere, except on the wall, where the magnetic field of the probe is imposed. The external magnetic field is generated by a single rectangular coil, with a negligible cross section of the wire, where an electric current flows. This geometry is quite common in clinical practice [43–46]. The analytical expression for the magnetic induction field is derived as in [47].

The analytical expression for the magnetic induction field is derived. A point in the coil reference frame, whose origin is at its center, is identified by the coordinates (x', y', z'). The coil dimensions are $2a_1$ along the x' axis and $2b_1$ in the y' direction. The axis z' is normal of the coil surface. The components of the magnetic induction field are

$$B_{x'} = \frac{\mu_0 I_1}{4\pi} \sum_{a=1}^{4} \left[\frac{z'(-1)^{a+1}}{r_a \left[r_a + d_a \right]} \right] \tag{13}$$

$$B_{y'} = \frac{\mu_0 I_1}{4\pi} \sum_{a=1}^{4} \left[\frac{z'(-1)^{a+1}}{r_a \left[r_a + C_a(-1)^{a+1} \right]} \right] \tag{14}$$

$$B_{z'} = \frac{\mu_0 I_1}{4\pi} \sum_{a=1}^{4} \left[\frac{d_a(-1)^a}{r_a \left[r_a + C_a(-1)^{a+1} \right]} - \frac{C_a}{r_a \left[r_a + d_a \right]} \right] \tag{15}$$

with

$$\begin{cases} C_1 = -C_4 = a_1 + x' \\ C_2 = -C_3 = a_1 - x' \\ d_1 = d_2 = y' + b_1 \\ d_3 = d_4 = y' - b_1 \\ r_a = \sqrt{C_a^2 + d_a^2 + z'^2} \end{cases} \tag{16}$$

The magnetic probe is located 1cm above the patient skin, in order for its modulus to be smaller than 1.5T, which is the limit allowed in clinical treatments [48], since higher values can cause damage to the patient. The liver is the target

8

	$Normal$	$CoilCoords$(m)	$TargetCoords$(m)	$B_z|_{1cm}$(mT)
$1^{st}run$	$n_x = 0.05899$	$x_{c,1} = 0.003678$	$x_{t,1} = 0.9983$	
	$n_y = 0.94519$	$y_{c,1} = -0.12346$	$y_{t,1} = -0.056$	46.21
	$n_z = 0.32114$	$z_{c,1} = -0.14145$	$z_{t,1} = -0.019$	
$2^{nd}run$	$n_x = 0.05899$	$x_{c,2} = 0.003678$	$x_{t,2} = 0.9983$	
	$n_y = 0.94519$	$y_{c,2} = -0.12346$	$y_{t,2} = -0.056$	-46.21
	$n_z = 0.32114$	$z_{c,2} = -0.14145$	$z_{t,2} = -0.019$	
$3^{rd}run$	$n_x = 0.05303$	$x_{c,3} = 0.001322$	$x_{t,3} = 0.9986$	
	$n_y = 0.97961$	$y_{c,3} = -0.12699$	$y_{t,3} = -0.052$	46.21
	$n_z = 0.19377$	$z_{c,3} = -0.12485$	$z_{t,3} = -0.0103$	
$4^{th}run$	$n_x = 0.05303$	$x_{c,4} = 0.001322$	$x_{t,4} = 0.9986$	
	$n_y = 0.97961$	$y_{c,4} = -0.12699$	$y_{t,4} = -0.052$	-46.21
	$n_z = 0.19377$	$z_{c,4} = -0.12485$	$z_{t,4} = -0.0103$	

Table 1: Source and target coordinates; values for the normal to the abdomen surface of the patient; intensity of the Magnetic field along the z-axis.

H_D(cm)	W_D(cm)	D_D(cm)	D_{M-T}(cm)	T_O(s)	Re_m
17.1	4.0	8.37	12	2	1097

Table 2: Simulation Parameters: H_D (domain height), W_D (domain width), D_D (domain depth), D_{S-T} (magnet-tumor distance), T_O (observation time), Re_m (mean aortic Reynolds number).

of the magneto-therapy, and the maximum magnetic field must be concentrated on it. Therefore, the distance between the origin of the probe and the target must be parallel to the z' axis.

The external abdominal surface of the patient is reconstructed using VMTK with the procedure previously illustrated for the arteries, and the two geometries are located in the same reference frame in order to calculate the coordinates of the probe and the target. The dimensions of the rectangular coil, the current intensity and the positions of coil and target can be found in Tab.(1), while the main simulation parameters are reported in Tab.(2)

2.6. Numerical Details

The simulations have been performed using the OpenFOAM code, which solves the governing equations though the Finite Volume Method (FVM). Despite the software offers a variety of precompiled solvers, the solution of the present problem required the implementation of a new one, which couples the Lagrangian particle dynamics with the Eulerian MHD. We developed this solver and called it `mhdParticle4BFoam`. We also implemented new BCs in OpenFOAM through the utility `groovyBC`: the resistive BC and the Womersley profile at the inlet for the unsteady simulations, as well as the parabolic profile for

the steady state ones. We also developed a new BC for the magnetic probe in an external module, called `rectMagProbe`. The simulations are carried on for 2 cardiac cycles, considering a period of 1s and a variable time step, in order to guarantee a Courant number always smaller than 0.5.

3. Results and Discussion

3.1. Solver Validation

The solver `mhdParticle4BFoam` couples the Lagrangian particle dynamics with the Eulerian MHD. A far as the MHD equations are concerned, there are few numerical solutions for channel [3], and pipe flow [4, 5]. As far as the Lagrangian particle dynamics is concerned, an analytical solution for the motion of a single particle moving in a viscous fluid in the presence of an external magnetic field can be found only under four restrictive hypothesis: (i) the particle is initially at the center of a channel whose width is much larger than its height and where the velocity gradient and the induced magnetic field are zero; (ii) the magnetic field applied is uniform; (iii) the flow is fully developed; (iv) the particle Reynolds number is small. Calling u_p, v_p, w_p respectively the axial, vertical and span-wise particle velocities and B_0 the external uniform magnetic field, applied in the vertical direction, Eq.(5) reduces to:

$$\begin{cases} \left(1 + \frac{1}{2}\frac{\rho_b}{\rho_p}\right)\frac{du_p}{dt} \approx -\frac{1}{\tau_p}\left(u_p - U_{\max}\right) - \frac{q_p}{m_p}B_0 w_p \\ \left(1 + \frac{1}{2}\frac{\rho_b}{\rho_p}\right)\frac{dv_p}{dt} \approx -\frac{1}{\tau_p}v_p - \left(1 - \frac{\rho_b}{\rho_p}\right)g \\ \left(1 + \frac{1}{2}\frac{\rho_b}{\rho_p}\right)\frac{dw_p}{dt} \approx -\frac{1}{\tau_p}w_p + \frac{q_p}{m_p}B_0 u_p \end{cases} \tag{17}$$

and defining:

$$\begin{cases} \tau_r = \tau_p\left(1 + \frac{1}{2}\frac{\rho_b}{\rho_p}\right) \\ \omega_B = \frac{q_p B_0}{m_p}\left(1 + \frac{1}{2}\frac{\rho_b}{\rho_p}\right)^{-1} \\ u_{p,\infty} = U_{\max}\left(1 + (\omega_B\tau_r)^2\right)^{-1} \\ v_{p,\infty} = -\tau_p\left(1 - \frac{\rho_b}{\rho_p}\right)g \\ w_{p,\infty} = \omega_B\tau_r U_{\max}\left(1 + (\omega_B\tau_r)^2\right)^{-1} \end{cases} \tag{18}$$

we obtain:

$$\begin{cases} u_p(t) \approx u_{p,\infty} - (u_{p,\infty} - u_{p,0})\,e^{-\frac{t}{\tau_r}}\cos(\omega_B t) + (w_{p,\infty} - w_{p,0})\,e^{-\frac{t}{\tau_r}}\sin(\omega_B t) \\ v_p(t) \approx v_{p,0}e^{-\frac{t}{\tau_r}} + v_{p,\infty}\left(1 - e^{-\frac{t}{\tau_r}}\right) \\ w_p(t) \approx w_{p,\infty} - (w_{p,\infty} - w_{p,0})\,e^{-\frac{t}{\tau_r}}\cos(\omega_B t) - (u_{p,\infty} - u_{p,0})\,e^{-\frac{t}{\tau_r}}\sin(\omega_B t) \end{cases} \tag{19}$$

The comparison between the theories can be seen in Fig.(3). The agreement between the theory and simulation is quite good, especially for the Eulerian
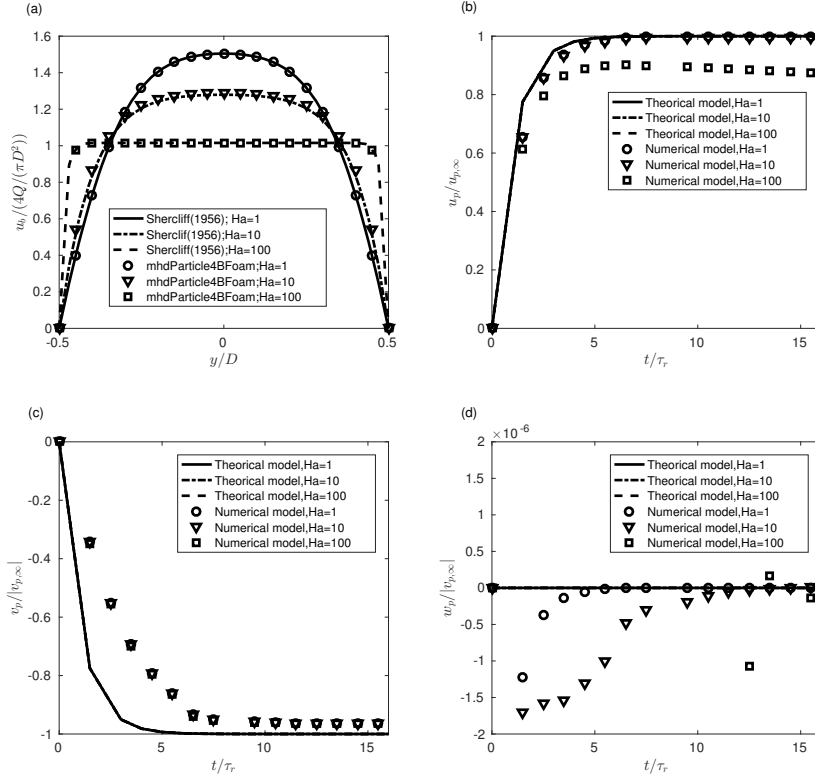
10

Figure 3: Solver validation tests. (a) numerical axial velocity vs theoretical axial velocity from [3]; (b) numerical particle axial velocity vs theoretical velocity from Eq.(19); (c) numerical particle vertical velocity vs theoretical velocity from Eq.(19); (d) numerical particle span-wise velocity vs theoretical velocity from Eq.(19).

part, i.e. Fig.(3,a). As far as the Lagrangian part is concerned, the agreement is good for the axial and vertical velocities, except for high Hartmann numbers, i.e. $Ha = 100$. For the span-wise velocity, as Fig.(3,d) shows, the agreement is less satisfactory. However, it must be noted that the span-wise velocity is much smaller than the settling velocity v_s, so the absolute numerical error is quite small. Further details on the validation can be found in [49].

3.2. Steady State Simulations

The steady state simulations are carried out until convergence is reached with the `simpleFoam` solver of OpenFOAM, which solves the Navier-Stokes equations in steady state. The results of the three meshes, i.e. grid1, grid2, grid3, are compared using the utility `mapFields` of OpenFOAM, which maps the fields from one grid to another. The wall shear stress (WSS), defined as

$$
\tau_{wall} = \hat{\vec{i}}_{axis} \cdot \rho_b \nu_b \left([I] - \hat{n}_{wall} \otimes \hat{n}_{wall}\right) \left([\nabla \vec{v}_b] + [\nabla \vec{v}_b]^T - \frac{2}{3} \operatorname{div}(\vec{v}_b)[I]\right)_{wall} \hat{n}_{wall}
\tag{20}
$$

is used to evaluate the grid independence. The contours of WSS are shown in Figure 4. The maximum WSS increases from grid1 to grid2, which means that grid1 has not enough resolution to resolve the velocity gradients. As far as grid2 and grid3 are concerned, the WSS values do not change significantly. Therefore, grid2 is employed to perform the unsteady simulations, being a compromise between speed of execution and accuracy.

Figure 4 shows that the WSS is low in the Aorta, due to the small velocity gradient, growing in the coeliac trunk and reaching the maximum in the LGA. In proximity of a bifurcation, or in presence of a bending, the WSS increases. Near the bifurcation of the coeliac trunk, the laminar flow impinges on the endothelial, and consequently the bifurcation is subject to higher WSS. The same behavior is also visible near the second bifurcation, where the coeliac trunk is subdivided in three branches: the LGA, CHA and SA. Overall, the order of magnitude of the WSS seems to be the same in all the branches of the coeliac trunk. This is due to the fact that the flow rate decreases with the section, in agreement with the literature [40–42]. Some exception can be seen in the LGA, where local peaks of WSS can be observed due to the presence of high curvature segments.

3.3. Unsteady State Simulations without external magnetic field

The unsteady simulations without external magnetic field are carried out by fixing the value of the current intensity to zero. As far as the inlet velocity is concerned, the pulsatile blood profile, derived from the Womersley equation, is imposed.

Figure 5 shows the time variations of the pressure field on the artery wall, which is representative of the pressure inside the whole domain at six different time steps of the cardiac cycle. The pressure variations during the cardiac cycle are very small, about 6mmHg. This is mostly due to the fact that the portion

(a) n = 174619; (b) n = 375972; (c) n = 724779;
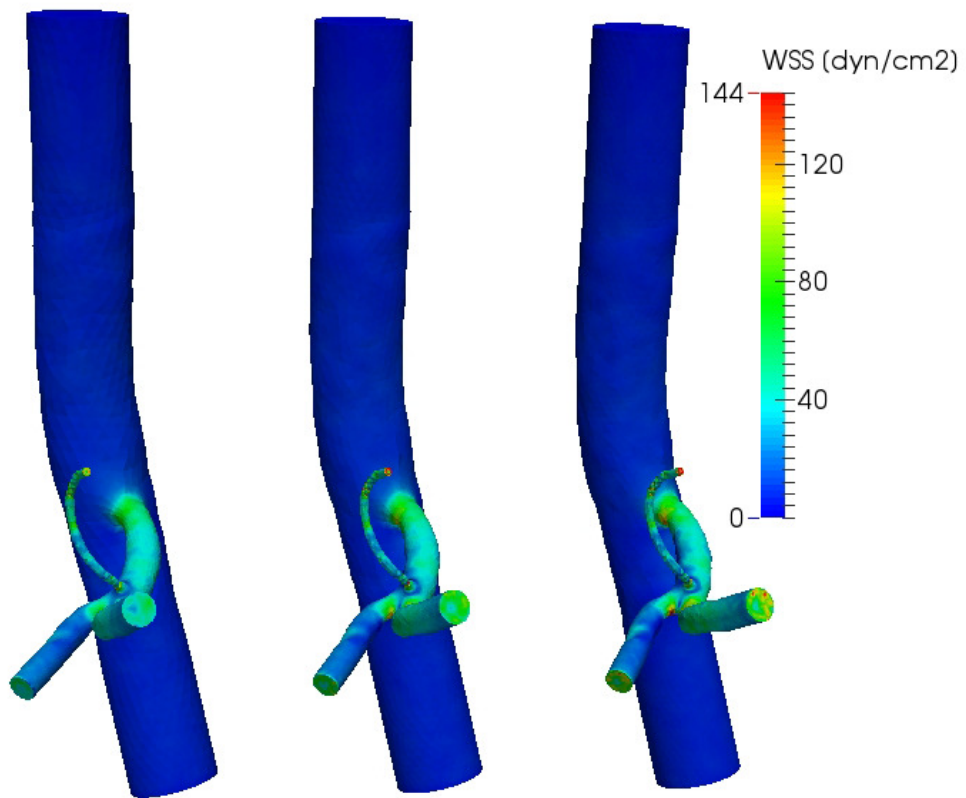
WSS (dyn/cm2)

144

120

80

40

0

Figure 4: WSS field for the grid independence study in steady state conditions.
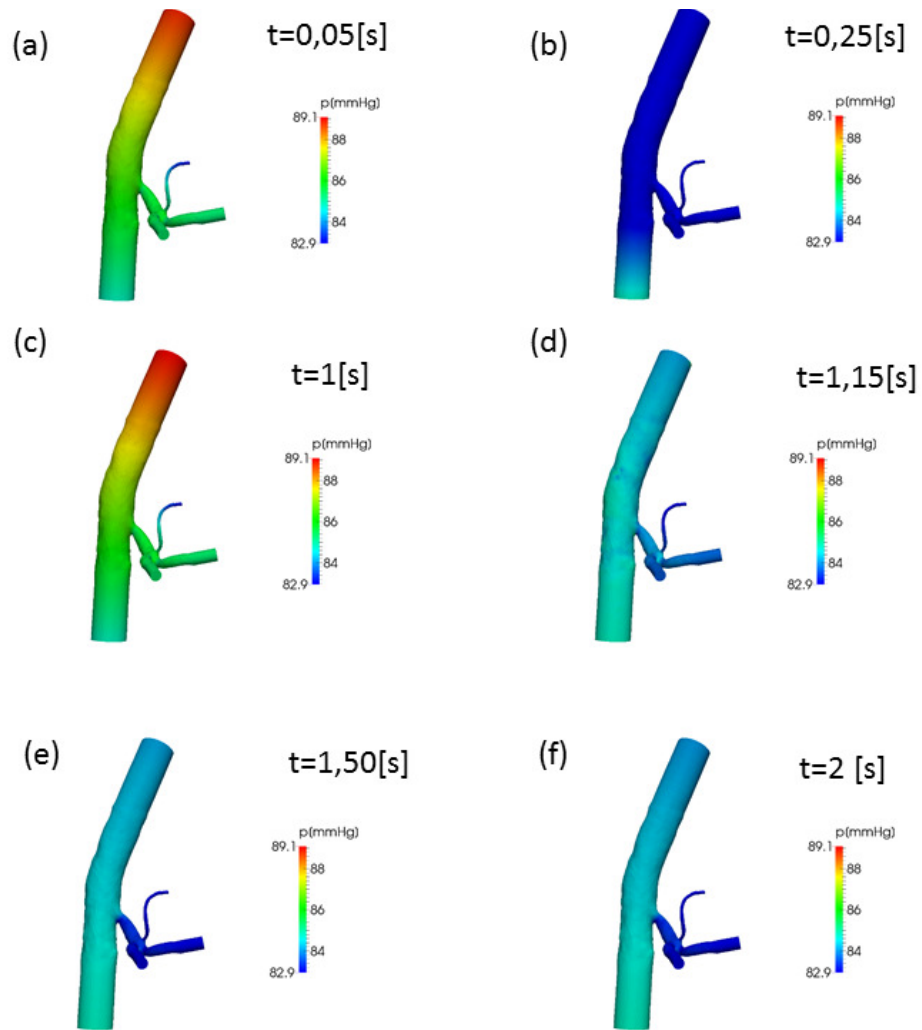
Figure 5: Unsteady Pressure field at different time-steps in absence of external magnetic field.

of the circulatory system considered is limited and, therefore, the pressure drop is small. Furthermore, on average, the pressure is higher in the Aorta than in the coeliac trunk and the lowest values are reached inside the Hepatic Artery, at the end of the cardiac cycle. This is due to the fact that in the coeliac trunk the radius of the artery decreases considerably and therefore there is a high pressure drop between this vessel and the Aorta.

Figure 5,a presents the pressure field in the Aorta at 0.05s, which is maximum because it is in the systolic phase and the blood flows from the atria to the ventricles. At 1s, Fig.(5,c) shows that the blood is ejected from the cardiac chambers, so the pressure in the Aorta is the highest. At 1.15s, Fig.(5,d) reports that the pressure is smaller in the Aorta because it is at the beginning of the diastolic phase, and finally, between 1.5s and 2s, i.e. in the last part of the diastolic phase, the pressure increases again in the Aorta and reaches the lowest value inside the Hepatic artery.

The WSS in absence of external magnetic field is reported in Fig.(6). Because of the periodicity of the profile, only some meaningful instants of time are shown. The WSS presents a periodic pattern, which depends on the cardiac cycle. In the last part of the systolic phase, described in Fig.(6,a), the ventricles are filled up with blood. The velocity in the Aorta is smaller and the WSS is higher only near the bifurcations or inside the bending branches, because some reversed flow is present and consequently the WSS changes direction. In both bifurcations and bends, the WSS is higher in the regions of the endothelium, where there is fluid impingement, and lower where a detachment of the fluid vein is present. As the cardiac cycle proceeds, the trend of the WSS remains the same.

3.4. Unsteady State Simulations with external magnetic field

The results of the particle motion in blood flow when the magnetic probe is turned on are presented in this section. Two positions of the coil and the target are investigated, as well as the sign of the current intensity, which makes 4 cases studied.

Table 1 shows the coordinates of coil and target point, as well as the intensity of the magnetic induction field, evaluated at 1cm on the axis from the center of the coil.

The maps of the magnetic field on the artery wall are shown in Figure 7 at two different time steps, i.e. $t = 1.5$s and $t = 2$s when the particles have filled the entire domain, and for the four different conditions presented in Table 1. The maximum value of the magnetic induction field is located close to the liver, where the probe is directed, and as a consequence, the particles tend to be dragged towards the coeliac trunk. The first conclusion derived from the 4 cases analyzed is that the sign of the current intensity has a minor influence on the solution, while the distance between the coil and the target is the parameter which affects mostly the particle dynamics.

The particle path-lines at $t = 1.25$s and $t = 1.5$s are shown in Figure 8 for the four different conditions described in Table 1. It appears that the flow is subject to a laminarization process. The particles on the center of the common
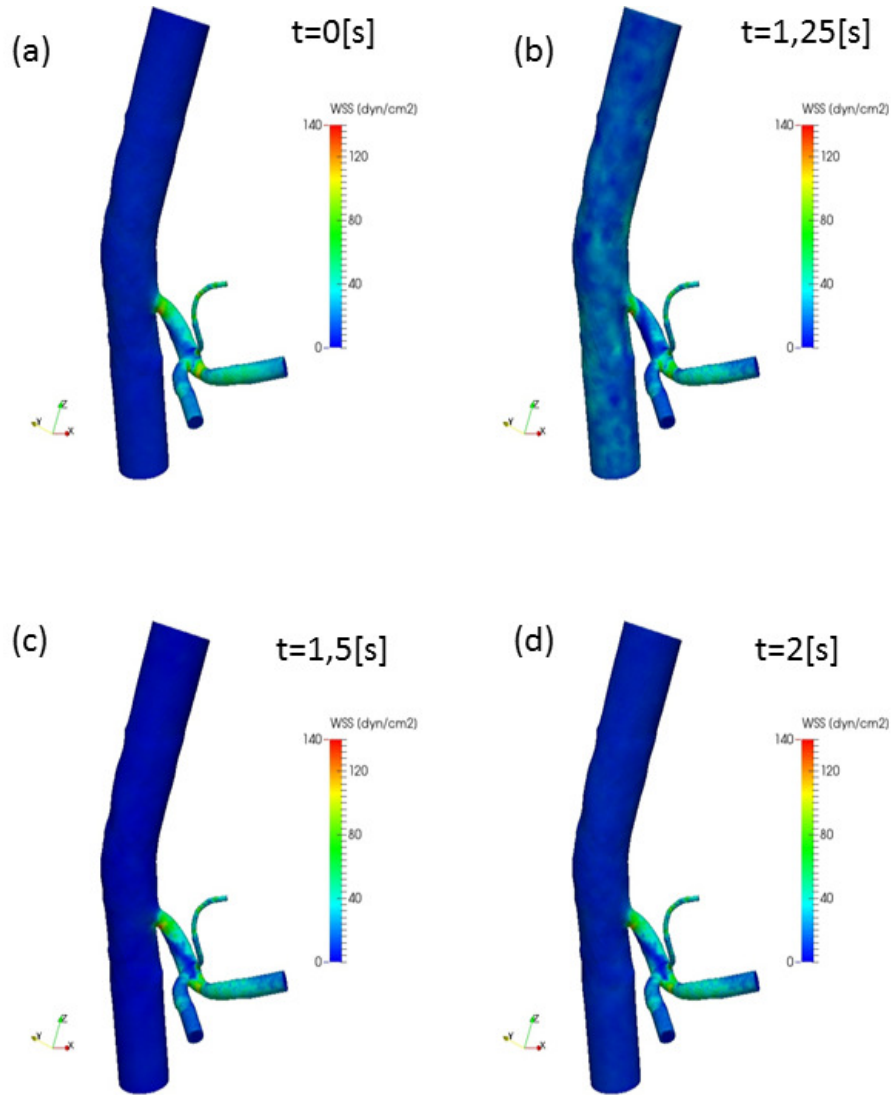
Figure 6: Unsteady WSS at different time-steps in absence of external magnetic field.
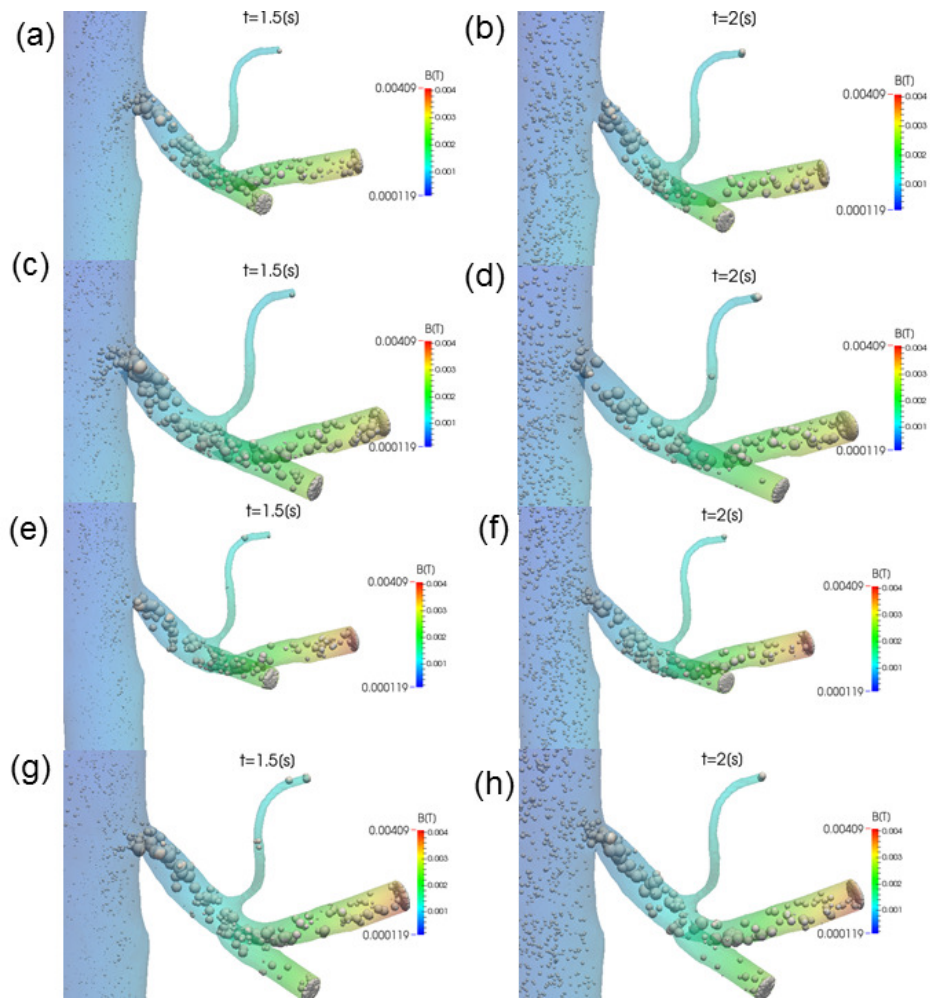
Figure 7: Magnetic Induction Field and particle positions at different time steps, for the different conditions listed in Table 1. (a) 1st run t = 1.5s; (b) 1st run t = 2s; (c) 2nd run t=1.5s; (d) 2nd run t= 2s; (e) 3rd run t = 1.5s; (f) 3rd run t = 2s; (g) 4th run t=1.5s; (h) 4th run t= 2s.
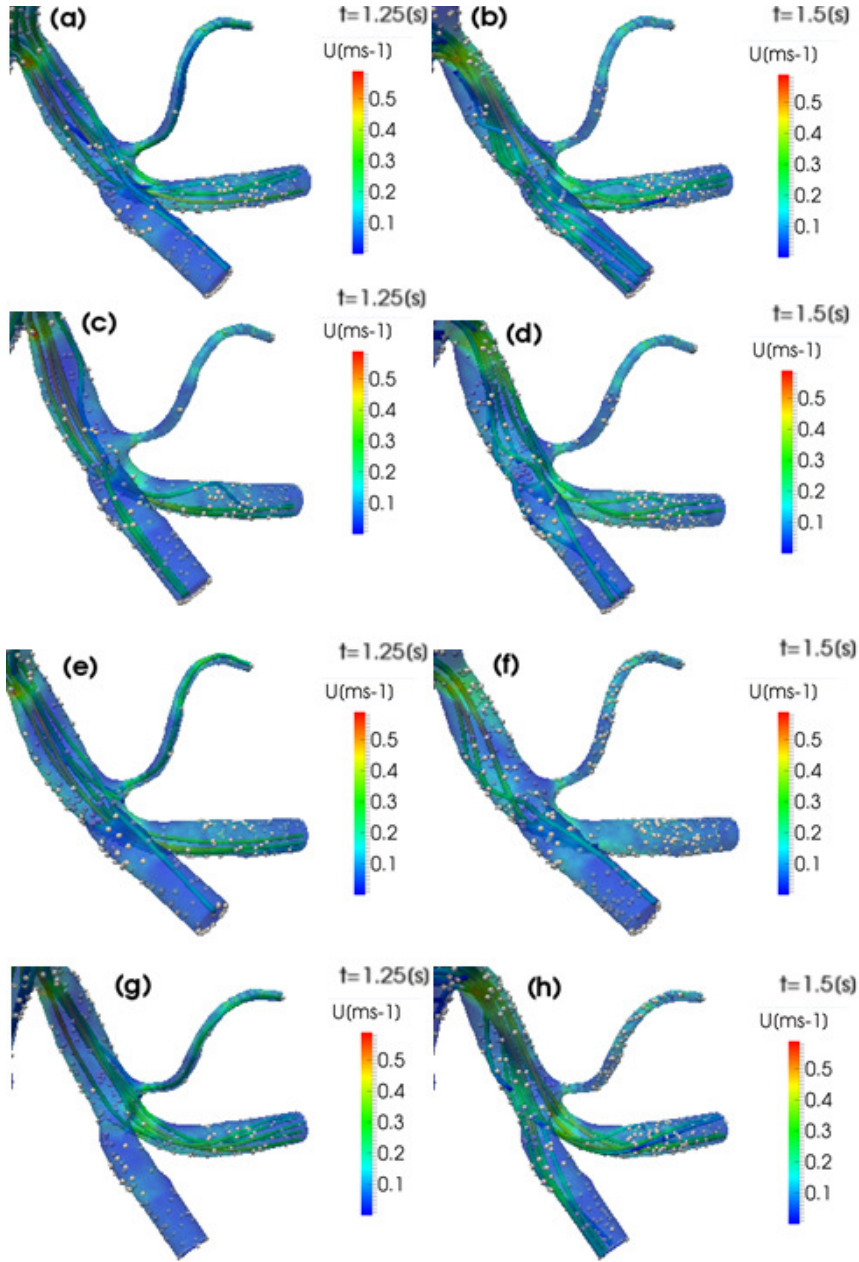
17

Figure 8: Velocity Field, particle positions and velocity vectors at different time steps, for the different conditions listed in Table 1. (a) 1st run t = 1.5s; (b) 1st run t = 2s; (c) 2nd run t=1.5s; (d) 2nd run t= 2s; (e) 3rd run t = 1.5s; (f) 3rd run t = 2s; (g) 4th run t=1.5s; (h) 4th run t= 2s.

18

coeliac trunk tend to go into the CHA, except at $t = 1.25$s, i.e. on the systolic peak, when the velocity is so high that they miss the CHA and flow directly into the SA and LGA. At $t = 1.5$s, i.e. in the diastolic phase, the particles tend to be deflected towards the bottom side of the coeliac trunk, and then transported into the CHA. The path-lines show a helical motion which begins at the point where the CHA originates, contributing to the increase of the local pressure drop. Moreover, the different positions of the probe and the different sign of the current intensity do not seem to influence the velocity field.

Figures 9 and 10 show the influence of the magnetic field on the absorption of the particles. To put in evidence the phenomenon, also the results with the magnetic probe turned off are reported.

Figure 9 shows the number of particles crossing a given surface per unit time during the cardiac cycle. This variable corresponds to the particle flow rate per unit volume. In the TA and in the domain wall the particle flow rates are of the same order of magnitude. A peak is present around 1s because the blood is ejected from the ventricles in the Aorta and there is a higher number of particles inside the artery. Afterwords, the particles flow rate decreases due to the diastolic phase. The comparison of Fig.(9,a) and Fig.(9,f) shows that the particles flow rates in those regions do not seem to be influenced by the parameters used in Table 1. On the contrary, on the outlets and especially on the Hepatic Artery, it is possible to observe an increase of the particles flow, thanks to the applied magnetic field.

The results concerning the particle flow rate may not be enough to judge the effectiveness of the use of a rectangular coil in the magnetic targeting. Therefore, the time integration of the particle flow rate per unit volume has been done, which corresponds to the total number of particles that crossed a given section since the beginning of the process. Figure 10 shows that the number of particles is approximately the same for the five different conditions inside the TA and on the domain wall, confirming the results shown in Figure 9. On the other hand, the results concerning the outlets show that the magnetic field influences the solution, because the number of particles increases in the LGA, CHA and SA, while it decreases in the AA. The CHA seems to be the branch which is mostly influenced by the presence of the probe. Depending on the position of the coil, the number of particle dragged into this vessel can increase twice or three times compared to the base case, when the probe is turned off. In particular, the last two cases of Table 1 represent the optimal conditions for the therapy, because they maximize the absorption of the nano-drugs in the liver, and, consequently, they minimize the dispersion of the drug in undesired locations reducing the side effects of the therapy.

4. Conclusions

The present work investigates via CFD the dynamics of nanoparticles in blood flow during magnetic drug delivery. This technique is emerging as a valid alternative to chemotherapy because of the reduced side effects. Due to the complexity of the problem, which requires the coupling of the blood flow with
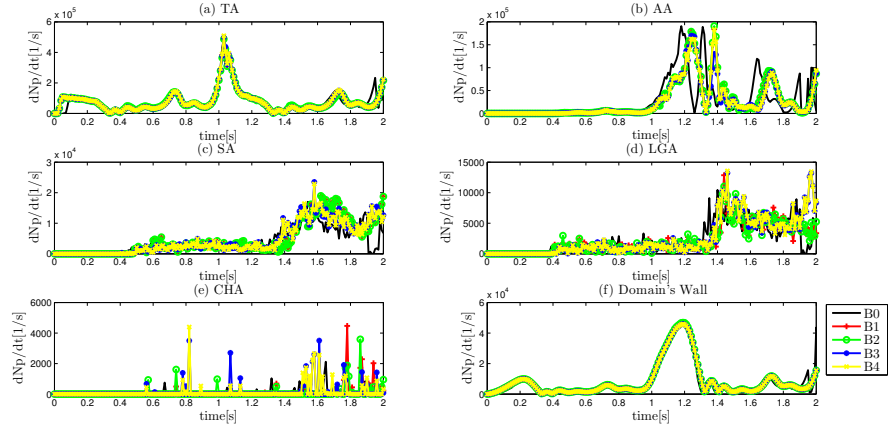
Figure 9: Particle volumetric flow rate per unit volume vs time for the different conditions in Table 1. B0 = no magnetic field; B1 = 1st run; B2 = 2nd run; B3 = 3rd run; B4 = 4th run.
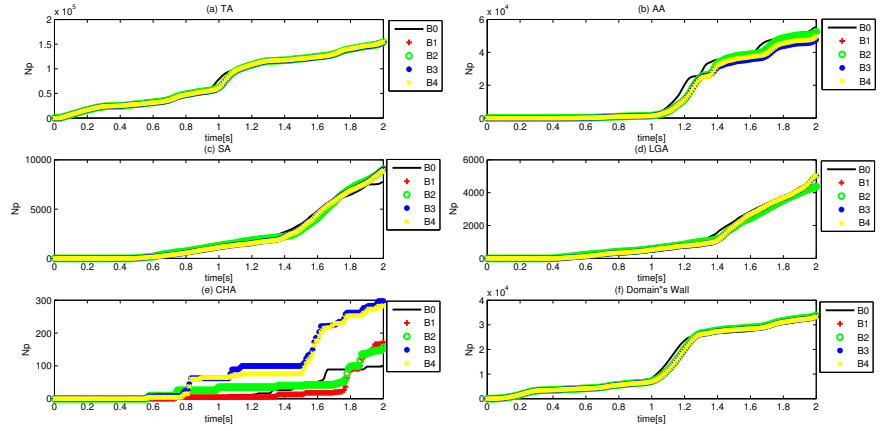

Figure 10: Particle number vs time for the different conditions in Table 1. B0 = no magnetic field; B1 = 1st run; B2 = 2nd run; B3 = 3rd run; B4 = 4th run.

the nanoparticles dynamics under the influence of an external magnetic field, there are a few numerical studies on this subject [25–30].

The purpose of this work is to verify via numerical simulations the effectiveness of this technique in the treatment of hepatic cancer. As every numerical study, this is subject to the limitations due to the input parameters and the model chosen. Nevertheless, the present hypothesis allows to describe accurately the phenomena, at least from a qualitative point of view.

The numerical simulations, for steady and unsteady states, are carried out with OpenFOAM, hypothesizing laminar flow, Newtonian viscosity for the blood and absence of inter and intra particle forces, due to the small size of the drug carriers. The simulations are carried out in a patient specific geometry, reconstructed from CT slices with VMTK. Three routines are employed in Open-FOAM to implement the BCs for the resistive pressure, the Womersley velocity profile and the magnetic field from the rectangular coil. Furthermore, a solver coupling the Eulerian MHD of the blood with the Lagrangian motion of particles is developed.

One simulation with the magnetic probe turned off and four with two different current intensities and two positions of the coil are carried out. The results are compared in order to find the best configuration which maximizes the intake of drug in the liver and consequently minimizes the dispersion in other locations. The rectangular coil, pointing perpendicularly to the liver is positioned in two points 1cm above the abdomen, and in two.

The results of the present numerical simulations show that the position of the probe highly influences the intake in the CHA. Nevertheless, despite the absolute number of particles flowing in this vessel can double or triple, it is still a very small fraction of the total number of particles injected.

In all the cases studied, only a minimal amount of the drug injected, about 0.2% in the CHA, 3.3% in the LGA and 6.6% in the SA, goes to the liver after 2 seconds from the beginning of the technique. About half of the injected drug is absorbed by the arterial wall, and the rest flows away through the AA. It was impossible to investigate all the possible positions of the target on the abdomen but it seems unlikely to increase significantly the drug intake in the liver by changing the position of the probe.

This conclusion is in agreement with [27, 28], but in contrast with the numerical findings of [26] for brain tumors. This is probably due to the closer distance between the magnet and the tumor (3cm), the larger particle diameter (2μm), and the higher magnetic field ($1 - 4$T). Magnetic drug delivery is extremely sensitive to these parameters, it shouldn't be surprising that the technique performs differently in different conditions.

The low performance of the magnetic drug delivery in the present study can be due to three factors: (i) the nanoparticle size; (ii) the magnet-tumor distance; (iii) the probe design. As far as the nanoparticle size is concerned, as shown in Eqs.(18-19) a low particle diameter increases the acceleration due to the Lorentz force, but it also increases the friction. However, because of the low magnetic field applied [50, 51] the effect on the friction is predominant. Therefore, larger particles should increase the effectiveness of the technique.

The probe-tumor distance is another factor which limits the effectiveness of the technique. Unfortunately, this parameter cannot be tuned at will. If the tumor is superficial, the magnetic drug targeting is likely to be more effective.

Finally, the design of the magnetic probe is another factor which influences the outcome of the procedure. This conclusion was suggested in [28] as well, where it was found that the sticking of particles to vessels occurred because of low blood flow velocity near the vessel walls, and this was suggested to be the main reason for low targeting efficiency.

The modulus of the magnetic induction field of a single rectangular coil decreases considerably with the distance from the target, i.e. the liver. Being the liver about 12cm far from the source, it is clear that this makes the modulus of the magnetic induction considerably low. A solution to this problem could be to increase the value of the current intensity flowing in the probe, but this is not possible because higher values of the magnetic field could affect the health of the patient, which is why this is forbidden by law [50, 51].

A different solution could be the employment of a different type of probe, which must focalize most of the energy on its axis in order to reduce the rate of decay of the magnetic field. Moreover, a possible configuration with multiple probes, positioned in appropriate locations, could also focus a higher magnetic field inside the target and limit the dangerous values of $\vec{B}$ elsewhere. A different solution, based on the use of a time-varying magnetic field, was proposed in [28] and showed a significant decrease in particle adherence to walls.

CFD allows detailed visualization of biological fluid flows, which increases our understanding of natural phenomena. Yet, CFD has some limitations due to the computational resources required to simulate a process in a complex domain. The question then arises as to whether or not the observation time (2s) is sufficient to judge the effectiveness of the technique. It would be certainly better to extend the simulations to a few minutes, but the particle volumetric flow rate in Fig.(9) at the different cases show negligible differences. It seems unlikely that the percentage of injected particles which reach the liver will significantly increase over time. Nevertheless, the liver uptake could increase, if the aortic wall would be saturated with nanoparticles. A few works have studied this problem [52–54] finding that the nanoparticle uptake is reduced for a concentration of a few μg/ml. In this work we used a Lagrangian approach to simulate the nonparticles flow, so the particle concentration is not directly available. However, we can derive an average concentration by multiplying the total number of particle injected by the mass of a single particle and dividing it by the domain volume. After 2s we obtain an average particle concentration of about $10^{-9}mg/ml$ which is far below the saturation limit. For a particle with $d_p = 500$nm the saturation limit would be reached in 3 minutes, but with the particle diameter used in this work, the saturation would not occur during the time frame of the procedure. Moreover, the particle release from the wall was allowed for in few numerical studies, e.g. [27, 30], but this didn't result in a significant increase in particle penetration into the tumor. In conclusion it is unlikely that extending the simulation time would change significantly the predicted efficiency of the technique.

Further numerical simulations, in different geometries and with different probes, are planned to assess the effectiveness of the therapy in different conditions.

5. Acknowledgments

References

[1] I. A. for Research on Cancer, W. H. Organization, et al., GLOBOCAN: Estimated Cancer Incidence, Mortality, and Prevalence Worldwide in 2012, IARC, 2014.

[2] J. Hartmann, F. Lazarus, Hg-dynamics II: Experimental investigations on the flow of mercury in a homogeneous magnetic field, Levin & Munksgaard, 1937.

[3] J. Shercliff, The flow of conducting fluids in circular pipes under transverse magnetic fields, Journal of Fluid Mechanics 1 (1956) 644–666.

[4] J. Shercliff, Magnetohydrodynamic pipe flow part2. high hartmann number, Journal of Fluid Mechanics 13 (1962) 513–518.

[5] R. R. Gold, Magnetohydrodynamic pipe flow. part 1, Journal of Fluid Mechanics 13 (1962) 505–512.

[6] W. R. Adey, Biological effects of electromagnetic fields, Journal of cellular biochemistry 51 (1993) 410–416.

[7] E. Tzirtzilakis, A mathematical model for blood flow in magnetic field, Physics of Fluids 17 (2005) 077103.

[8] Z. Saiyed, S. Telang, C. Ramchand, Application of magnetic techniques in the field of drug discovery and biomedicine, BioMagnetic Research and Technology 1 (2003) 2.

[9] M. A. Ikbal, S. Chakravarty, K. K. Wong, J. Mazumdar, P. K. Mandal, Unsteady response of non-newtonian blood flow through a stenosed artery in magnetic field, Journal of Computational and Applied Mathematics 230 (2009) 243–259.

[10] F. Gori, A. Boghi, M. Amitrano, Three-dimensional numerical simulation of the fluid dynamics in a coronary stent, in: ASME 2009 International Mechanical Engineering Congress and Exposition, American Society of Mechanical Engineers, 2009, pp. 407–411.

[11] F. Gori, A. Boghi, Image-based computational fluid dynamics in a carotid artery, in: ASME 2009 International Mechanical Engineering Congress and Exposition, American Society of Mechanical Engineers, 2009, pp. 123–128.

[12] F. Gori, A. Boghi, Three-dimensional numerical simulation of non-newtonian blood in two coronary stents, in: 2010 14th International Heat Transfer Conference, American Society of Mechanical Engineers, 2010, pp. 109–114.

[13] F. Gori, A. Boghi, Three-dimensional numerical simulation of blood flow in two coronary stents, Numerical Heat Transfer, Part A: Applications 59 (2011) 231–246.

[14] A. Boghi, F. Gori, Numerical simulation of blood flow through different stents in stenosed and non-stenosed vessels, Numerical Heat Transfer, Part A: Applications 68 (2015) 225–242.

[15] I. Di Venuta, A. Boghi, F. Gori, Three-dimensional numerical simulation of a failed coronary stent implant at different degrees of residual stenosis. part i: Fluid dynamics and shear stress on the vascular wall, Numerical Heat Transfer, Part A: Applications (2017,in press).

[16] A. Boghi, I. Di Venuta, F. Gori, Three-dimensional numerical simulation of a failed coronary stent implant at different degrees of residual stenosis. part ii: Apparent viscosity and wall permeability, Numerical Heat Transfer, Part A: Applications (2017,in press).

[17] X. Li, K. Yao, Z. Liu, Cfd study on the magnetic fluid delivering in the vessel in high-gradient magnetic field, Journal of Magnetism and Magnetic Materials 320 (2008) 1753–1758.

[18] L. Moulinier, T. Venet, N. B. Schiller, T. W. Kurtz, R. C. Morris, A. Sebastian, Measurement of aortic blood flow by doppler echocardiography: day to day variability in normal subjects and applicability in clinical research, Journal of the American College of Cardiology 17 (1991) 1326–1333.

[19] Q. Long, X. Xu, M. Collins, M. Bourne, T. Griffith, Magnetic resonance image processing and structured grid generation of a human abdominal bifurcation, Computer Methods and Programs in Biomedicine 56 (1998) 249–259.

[20] J. Haverkort, S. Kenjereš, C. Kleijn, Computational simulations of magnetic particle capture in arterial flows, Annals of biomedical engineering 37 (2009) 2436–2448.

[21] R. K. Jain, Delivery of molecular and cellular medicine to solid tumors, Advanced drug delivery reviews 46 (2001) 149–168.

[22] M. R. Habibi, M. Ghasemi, Numerical study of magnetic nanoparticles concentration in biofluid (blood) under influence of high gradient magnetic field, Journal of Magnetism and Magnetic Materials 323 (2011) 32–38.

[23] A. S. Lübbe, C. Alexiou, C. Bergemann, Clinical applications of magnetic drug targeting, Journal of Surgical Research 95 (2001) 200–206.

[24] A. S. Lübbe, C. Bergemann, H. Riess, F. Schriever, P. Reichardt, K. Possinger, M. Matthias, B. Dörken, F. Herrmann, R. Gürtler, et al., Clinical experiences with magnetic drug targeting: a phase i study with 4-epidoxorubicin in 14 patients with advanced solid tumors, Cancer research 56 (1996) 4686–4693.

[25] A. Nacev, C. Beni, O. Bruno, B. Shapiro, The behaviors of ferromagnetic nano-particles in and around blood vessels under applied magnetic fields, Journal of magnetism and magnetic materials 323 (2011) 651–668.

[26] S. Kenjereš, B. Righolt, Simulations of magnetic capturing of drug carriers in the brain vascular system, International Journal of Heat and Fluid Flow 35 (2012) 68–75.

[27] M. Larimi, A. Ramiar, A. Ranjbar, Numerical simulation of magnetic nanoparticles targeting in a bifurcation vessel, Journal of Magnetism and Magnetic Materials 362 (2014) 58–71.

[28] M. D. Tehrani, J.-H. Yoon, M. O. Kim, J. Yoon, A novel scheme for nanoparticle steering in blood vessels using a functionalized magnetic field, IEEE Transactions on Biomedical Engineering 62 (2015) 303–313.

[29] M. Larimi, A. Ramiar, A. Ranjbar, Numerical simulation of magnetic drug targeting with eulerian-lagrangian model and effect of viscosity modification due to diabetics, Applied Mathematics and Mechanics 37 (2016) 1631–1646.

[30] M. Momeni Larimi, A. Ramiar, A. A. Ranjbar, Magnetic nanoparticles and blood flow behavior in non-newtonian pulsating flow within the carotid artery in drug delivery application, Proceedings of the Institution of Mechanical Engineers, Part H: Journal of Engineering in Medicine 230 (2016) 876–891.

[31] D. A. Steinman, Image-based computational fluid dynamics modeling in realistic arterial geometries, Annals of biomedical engineering 30 (2002) 483–497.

[32] T. S. Tenforde, Magnetically induced electric fields and currents in the circulatory system, Progress in Biophysics and Molecular Biology 87 (2005) 279–288.

[33] S. Elghobashi, On predicting particle-laden turbulent flows, Applied scientific research 52 (1994) 309–329.

[34] E. Tzirtzilakis, V. Sakalis, N. Kafoussias, P. Hatzikonstantinou, Biomagnetic uid ow in a 3d rectangular duct, Int. J. Numer. Meth. Fluids 44 (2004) 1279–1298.

[35] M. Arruebo, R. Fernández-Pacheco, M. R. Ibarra, J. Santamaría, Magnetic nanoparticles for drug delivery, Nano today 2 (2007) 22–32.

[36] S. Seino, Y. Matsuoka, T. Kinoshita, T. Nakagawa, T. A. Yamamoto, Dispersibility improvement of gold/iron-oxide composite nanoparticles by polyethylenimine modification, Journal of Magnetism and Magnetic Materials 321 (2009) 1404–1407.

[37] L. Schiller, Z. Naumann, A drag coefficient correlation, Vdi Zeitung 77 (1935) 51.

[38] C. A. Taylor, T. J. Hughes, C. K. Zarins, Finite element modeling of three-dimensional pulsatile flow in the abdominal aorta: relevance to atherosclerosis, Annals of biomedical engineering 26 (1998) 975–987.

[39] L. Grinberg, G. E. Karniadakis, Outflow boundary conditions for arterial networks with multiple outlets, Annals of biomedical engineering 36 (2008) 1496–1514.

[40] R. W. Gill, Measurement of blood flow by ultrasound: accuracy and sources of error, Ultrasound in medicine & biology 11 (1985) 625–641.

[41] B. T. Tang, C. P. Cheng, M. T. Draney, N. M. Wilson, P. S. Tsao, R. J. Herfkens, C. A. Taylor, Abdominal aortic hemodynamics in young healthy adults at rest and during lower limb exercise: quantification using image-based computer modeling, American Journal of Physiology-Heart and Circulatory Physiology 291 (2006) H668–H676.

[42] M. Žáček, E. Krause, Numerical simulation of the blood flow in the human cardiovascular system, Journal of biomechanics 29 (1996) 13–20.

[43] M. A. Azpurua, A semi-analytical method for the design of coil-systems for homogeneous magnetostatic field generation, Progress In Electromagnetics Research B 37 (2012) 171–189.

[44] G. J. Metzger, P.-F. van de Moortele, C. Akgun, C. J. Snyder, S. Moeller, J. Strupp, P. Andersen, D. Shrivastava, T. Vaughan, K. Ugurbil, et al., Performance of external and internal coil configurations for prostate investigations at 7 t, Magnetic resonance in medicine 64 (2010) 1625–1639.

[45] F. Dughiero, E. Baake, M. Forzan, V. Nemkov, R. Ruffini, R. Goldstein, J. Jackowski, T. DeWeese, R. Ivkov, Magnetic field generating inductor for cancer hyperthermia research, COMPEL-The international journal for computation and mathematics in electrical and electronic engineering 30 (2011) 1626–1636.

[46] T. Takamura, P. J. Ko, J. Sharma, R. Yukino, S. Ishizawa, A. Sandhu, Magnetic-particle-sensing based diagnostic protocols and applications, Sensors 15 (2015) 12983–12998.

[47] M. Misakian, Equations for the magnetic field produced by one or more rectangular loops of wire, Journal of research of the National Institute of Standards and Technology 105 (2000).

[48] M. W. Wilson, R. K. Kerlan Jr, N. A. Fidelman, A. P. Venook, J. M. LaBerge, J. Koda, R. L. Gordon, Hepatocellular carcinoma: Regional therapy with a magnetic targeted carrier bound to doxorubicin in a dual mr imaging/conventional angiography suiteinitial experience with four patients 1, Radiology 230 (2004) 287–293.

[49] F. Russo, Numerical Simulation of MagnetoHydroDynamics inside cardiovascular and respiratory systems, Ph.D. thesis, Università degli Studi di Roma "Tor Vergata", 2015.

[50] C. Recommendation, 519/ec of 12 july 1999 on the limitation of exposure of the general public to electromagnetic fields (0 hz to 300 ghz), Official Journal of the European Communities L 59 (1999) 59–70.

[51] R. F. Cleveland, D. M. Sylvar, J. L. Ulcek, Evaluating compliance with FCC guidelines for human exposure to radiofrequency electromagnetic fields, Standards Development Branch, Allocations and Standards Division, Office of Engineering and Technology, Federal Communications Commission, 1997.

[52] C. Song, V. Labhasetwar, X. Cui, T. Underwood, R. J. Levy, Arterial uptake of biodegradable nanoparticles for intravascular local drug delivery: results with an acute dog model, Journal of Controlled Release 54 (1998) 201–211.

[53] V. Labhasetwar, C. Song, W. Humphrey, R. Shebuski, R. J. Levy, Arterial uptake of biodegradable nanoparticles: effect of surface modifications, Journal of pharmaceutical sciences 87 (1998) 1229–1234.

[54] J. Davda, V. Labhasetwar, Characterization of nanoparticle uptake by endothelial cells, International journal of pharmaceutics 233 (2002) 51–59.